

See discussions, stats, and author profiles for this publication at: <https://www.researchgate.net/publication/267867928>

Preparation, Structure, and Orientation of Pyrite $\text{FeS}_2\{100\}$ Surfaces: Anisotropy, Sulfur Monomers, Dimer Vacancies, and a Possible FeS Surface Phase

ARTICLE *in* THE JOURNAL OF PHYSICAL CHEMISTRY C · AUGUST 2014

Impact Factor: 4.77 · DOI: 10.1021/jp5005924

CITATIONS

2

READS

74

5 AUTHORS, INCLUDING:



Klas J. Andersson

Haldor Topsøe

34 PUBLICATIONS 1,264 CITATIONS

SEE PROFILE



Hirohito Ogasawara

Stanford University

142 PUBLICATIONS 5,171 CITATIONS

SEE PROFILE



Dennis Nordlund

Stanford University

186 PUBLICATIONS 4,617 CITATIONS

SEE PROFILE

Preparation, Structure, and Orientation of Pyrite $\text{FeS}_2\{100\}$ Surfaces: Anisotropy, Sulfur Monomers, Dimer Vacancies, and a Possible FeS Surface Phase

Klas J. Andersson,^{†,‡} Hirohito Ogasawara,[‡] Dennis Nordlund,[‡] Gordon E. Brown, Jr.,^{‡,§} and Anders Nilsson^{*,†,‡}

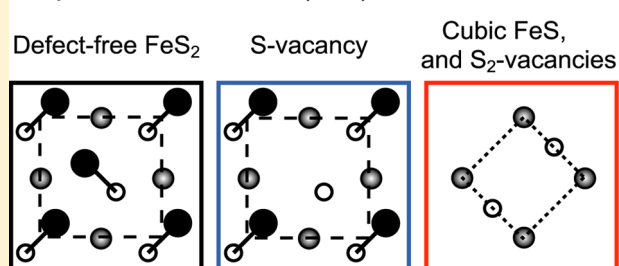
[†]FYSIKUM, Stockholm University, SCFAB, S-10691 Stockholm, Sweden

[‡]SLAC National Accelerator Laboratory, 2575 Sand Hill Road, Menlo Park, California 94025, United States

[§]Department of Geological and Environmental Sciences, Stanford University, Stanford, California 94305-2115, United States

ABSTRACT: Sulfur dimer (S_2^{2-}) terminated pyrite $\text{FeS}_2\{100\}$ surfaces with a low energy electron diffraction (LEED) pattern of 2×1 symmetry are reported. The 2×1 symmetry correlates with the orientation of the anisotropic surface structure and external symmetry of macroscopic striations on the pyrite cube face. The basic condition to form these surfaces is a mild 200 V Ne^+ sputter-cleaning procedure followed by a 570 K anneal of the sample in a 10^{-7} Torr $\text{S}_2(\text{g})$ atmosphere. Controlled amounts of surface sulfur monomers (S^{2-}) can be introduced by mild sputtering of the sulfur dimer terminated surfaces. At low monomer concentrations the surface displays the same characteristic 1×1 LEED pattern as that for fracture-generated surfaces. With increasing sulfur depletion, a $(1/\sqrt{2} \times 1/\sqrt{2})\text{R}45^\circ$ LEED pattern emerges, and soft X-ray photoelectron spectroscopy (XPS) results show a sulfur dimer deficient near-surface region and a new high binding energy sulfur spectral component suggesting the presence of local coordination environments where sulfur monomers are coordinated by four Fe ions compared to three as in the pyrite structure. The plausible formation of a defective FeS-like surface phase where monomeric sulfurs are coordinated by four Fe ions, and bond counting energetics favoring surface sulfur monomer recombination around Fe vacancy sites on pyrite $\text{FeS}_2\{100\}$, both imply surface sulfur dimer vacancy sites with unique adsorption and reactivity properties. Taken together, our results suggest a very rich and dynamic defect structural landscape at pyrite $\text{FeS}_2\{100\}$ surfaces with direct implications for its surface chemical activity.

Preparation and $\text{FeS}_2(100)$ surface structures



1. INTRODUCTION

Many aspects of pyrite reactivity have been studied extensively¹ in relation to photovoltaic applications² and mechanisms of oxidation resulting in generation of acid mine drainage and release of associated trace metals in aqueous environments around base-metal and precious-metal sulfide mines.^{3,4} It has also been suggested that pyrite FeS_2 surfaces have played a central role in the origin of life, acting as a catalyst and chiral discriminator in the formation of prebiotic molecules.^{5–7} The lowest free energy surface termination of pyrite, $\{100\}$, is also the most commonly found surface termination in natural habitats.^{8,9} It is also generated upon fracturing pyrite, which results in $\{100\}$ surfaces with macroscopic conchoidal to uneven morphology.

Depictions of defect-free bulk truncated and thus sulfur dimer (S_2^{2-}) terminated $\text{FeS}_2\{100\}$ surfaces, for which only Fe–S bonds are cleaved, are shown in Figure 1(a–c) along with a 1×1 surface unit cell and the $(1/\sqrt{2} \times 1/\sqrt{2})\text{R}45^\circ$ Fe^{2+} -sublattice surface unit cell. Shown in Figure 1(d) are the reciprocal surface sublattices of S_2^{2-} (1×1) and Fe^{2+} which we will discuss later in relation to the low energy electron diffraction (LEED) results. Structurally, the 3D crystal

symmetry of pyrite is that of space group $Pa\bar{3}$. Pyrite crystallizes in the cubic NaCl structure with Fe^{2+} in the Na^+ sites and dimer sulfur anions S_2^{2-} with center of mass located at the Cl^- sites. The molecular axes of the dimers are aligned along the four equivalent $\langle 111 \rangle$ directions, and in the bulk both sulfur atoms in the sulfur dimer anion are bonding to (coordinated by) three Fe^{2+} , i.e., have a Fe-coordination number (Fe_{CN}) of three. In each FeS_2 layer along a $\langle 100 \rangle$ direction only two out of the four S_2^{2-} orientations are represented, and this gives rise to two specific combinations of S_2^{2-} orientations, i.e., two types of FeS_2 layers that alternate along a specific $\langle 100 \rangle$ direction as can be seen in Figure 1(a), (b), and (c).

Bulk truncated sulfur dimer terminated $\text{FeS}_2\{100\}$ surfaces belong to the 2D space group pg with glide reflection [along $[010]$, i.e., b -glide symmetry, in Figure 1 (a) and (b)] as the only symmetry operation other than identity. The lack of mirror symmetry in the $\text{FeS}_2\{100\}$ surface plane [i.e., no mirror plane along $[001]$ (c -axis)] gives rise to surface chirality; i.e.,

Received: January 17, 2014

Revised: August 23, 2014

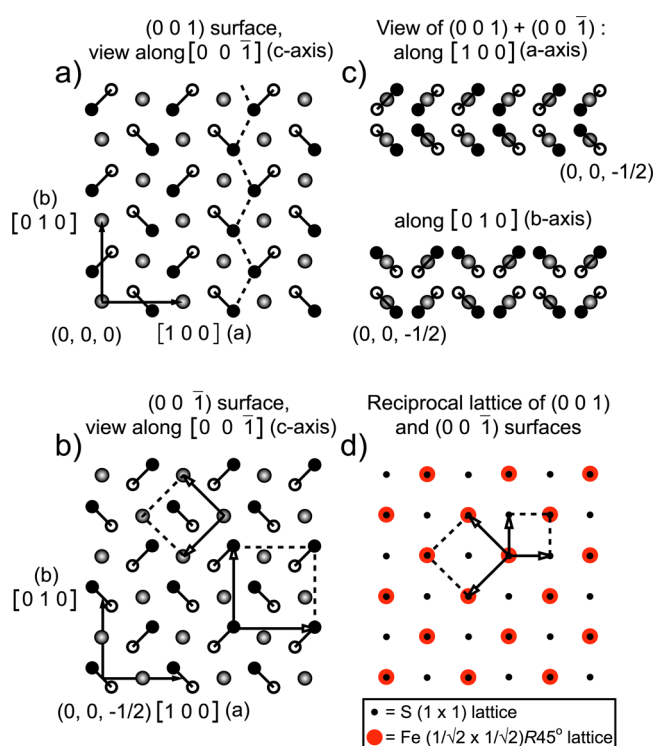


Figure 1. Views of bulk truncated sulfur dimer terminated pyrite $\text{FeS}_2\{100\}$ surfaces, S_2^{2-} and Fe^{2+} sublattices, and their corresponding reciprocal lattices for discussing the observed LEED patterns. Larger gray filled circles represent Fe atoms; black filled circles represent sulfur atoms closest to the viewer; and unfilled circles represent sulfur atoms further away from the viewer. Note the connecting line between sulfurs in dimers and that it can be used to judge the location of the dimer center of mass in front of or behind Fe atoms in the projections in (c). The surface anisotropy is illustrated in (a) using a dashed line along the vertical direction which emphasizes the zigzag nature of the troughs.

adsorption sites on $\text{FeS}_2\{100\}$ can be chiral discriminators toward chiral molecules. The (001) surface and (00 $\bar{1}$) surface, which are representative for the two types of FeS_2 layers in the [001] (*c*-) direction, are interrelated by a *c*-glide operation (along [00 $\bar{1}$] parallel to [100]). Both surfaces (FeS_2 layers) display lattice-sulfur induced valley and trough zigzag structures at the surface along the [010] direction (*b*-axis) but not in the [100] direction (*a*-axis) which is a direct result of the structural anisotropy in the bulk. This valley and trough structure only present along the *b*-axis is easiest observed in the side view of Figure 1(c) (bottom), and the zigzag nature is illustrated via the dashed line along the vertical direction in Figure 1(a); connected black filled and empty circles in Figure 1(a–c) are sulfur dimer atoms closer to and further away from the viewer, respectively. As discussed later in Section 2, the orientation of our pyrite single crystal is known and is such as shown in Figure 1(a) and (b) in relation to our observed LEED patterns. The correspondence between observed LEED patterns and the reciprocal lattices of the surface (see Figure 1(b) and (d)) allows us to discuss average symmetry and structural properties of the pyrite $\text{FeS}_2\{100\}$ near surface region.

Defects related to ruptured pyrite sulfur dimers leading to chemically active sulfur atom vacancy sites^{10–13} are naturally generated at $\text{FeS}_2\{100\}$ surfaces prepared by fracturing.¹¹ These defects are involved in the initial rapid surface oxidation of fracture surfaces under ambient conditions^{10,11,14,15} and

display unique activity toward biomolecules.¹³ Although expected to be significantly less reactive compared to surface sulfur atom vacancy sites, leaving a monomeric sulfur behind, surface Fe vacancies have also been documented by scanning tunneling microscopy (STM),¹⁶ with theoretically estimated formation energies similar to sulfur atom vacancies.¹⁷

XPS core-level shifts are highly sensitive to the local atomic level electronic structure, i.e., the nature of the chemical bonds, the bond distances, and the coordination number of the core ionized atom. Atomic-level insights regarding the structural nature of the above-discussed sulfur defects as well as other local sulfur structures at $\text{FeS}_2\{100\}$ surfaces were previously achieved by a combined theoretical and experimental study of the S 2p XP spectra of low sulfur monomer density and monomer-free surfaces,¹¹ prepared as described in detail in this paper. The high accuracy of the simple and chemically intuitive Z+1 approximation utilized in ref 11 to model the S 2p core level shifts (CLS) and the strict structural assignments obtained have since been verified at a higher level of theory.¹² The calculated relative pyrite S 2p CLS in refs 11 and 12 closely matches the experimental relative binding energies between no less than four local sulfur environments described here and in ref 11, spanning a wide binding energy range of 2.1 eV, and furthermore correctly predicts the experimentally observed trend of increasing binding energy shift between surface and bulk species by 0.1 eV when probing progressively deeper into the bulk and thereby probing bulk environments less affected by surface relaxation effects.¹¹ Additionally, the mild sputtering procedure in ref 11 induces the expected sulfur atom vacancies, in good agreement with their theoretically predicted CLSs relative to both bulk and surface dimer sulfur atoms. At the heart of the approximations used for calculating the CLS in refs 11 and 12 lays the assumption of an electronically fully screened core hole final state of lowest total energy, corresponding to an electronic structure adiabatic limit XPS line within the sudden approximation. This assumption holds true for the components of pyrite S 2p XP spectra which display no significant high binding energy (energy loss) satellite or shakeup structures.¹¹ However, pyrite Fe 2p XP spectra display a broad tail high binding energy region.^{1,14} Due to the open d-shell nature of Fe, spin–spin coupling gives rise to multiple competing Fe 2p XPS final states of similar spectral weight but differing energy.¹⁴ These complex surface Fe^{2+} and Fe^{3+} spin multiplet Fe 2p XPS final states were not accounted for in ref 12, and the inability to correctly model Fe 2p CLS in ref 12 should thus not be taken to illustrate any limitations of the methodology used for the quantitative modeling of S 2p CLS in refs 11 and 12.

Structural features and properties such as chirality, sulfur vacancies,^{10,11,14} steps,^{16,18} and the trough and valley type anisotropy^{18,19} are all present at $\text{FeS}_2\{100\}$ surfaces. These features all influence its adsorption properties which are relevant in processes such as flotation separation of pyrite from base-metal sulfide ore minerals,²⁰ surface oxidation,^{3,4} crystal growth kinetics,²¹ biomass attachment,^{22,23} and the possible role of pyrite in the origin of life in the iron–sulfur world scenario.^{5–7,13} Because of variations in observed reactivity of pyrite {100} surfaces, it is of great interest to find sample preparation conditions under which full control of pyrite surface defect density can be achieved. Furthermore, any additional insights into the surface structure of pyrite, which dictates its adsorption and reactivity properties, are important. In this work S 2p XPS and LEED were employed to

simultaneously monitor sulfur defect density and structure of $\text{FeS}_2\{100\}$ surfaces prepared in different manners. Besides the formation of a plausible FeS-like surface phase at severe surface sulfur depletion, under milder sulfur depletion pyrite sulfur dimer vacancies with expected unique reactivity at pyrite $\text{FeS}_2\{100\}$ surfaces are inferred on the basis of spectroscopic, structural, and energetic arguments.

2. EXPERIMENTAL SECTION

The experiments were performed at beamline I511 at the Swedish national synchrotron radiation facility MAX-lab in Lund, Sweden.²⁴ The vacuum chamber with a base pressure of 2×10^{-10} Torr during our experiments was equipped with a mass spectrometer, ion gun, SES-200 electron analyzer, and LEED optics. LEED measurements were performed slightly off-axis (azimuthal) due to the use of a $3\text{--}5^\circ$ grazing incidence of photons for photoemission, and the polar angle was close to 0° for the reported LEED images. The pyrite $\{100\}$ surfaces used were 1 cm^2 and 2 mm thick slices cut from cubic natural single crystals with a mirror finish from Navajun, Spain.

Macroscopic narrow striations parallel to $[010]$ (b -axis) in our coordinate system were visible on the naturally grown $\{100\}$ surfaces. Microtopographic studies of $\{100\}$ surfaces of the cubic form of pyrite have shown that the observed striations are associated with the piling-up process of edges of rectangular $\{100\}$ growth layers,^{8,9} in our coordinate system elongated along $[010]$ (b -axis). These macroscopic striations on the pyrite cube $\{100\}$ faces are correlated with the crystal structure²⁵ and are parallel with the lattice-sulfur induced trough and valley structures. By observing the direction of striations on the $\{100\}$ surface we know the orientation of our pyrite single crystal prior to experiments.

The samples were initially ultrasonically cleaned in acetone for 30 min, then in ethanol for 30 min, and subsequently lightly etched (3 drops 14 M HCl in 40 mL of H_2O for 2 min). After introduction into the ultra high vacuum chamber and initial sputter cleaning with 200 V Ne^+ (1 kV Ne^+ , +800 V sample bias) at 2 μA sample current to remove the bulk of the remaining surface contaminants, a 10 min sputtering procedure at the same conditions could then routinely eliminate residual surface contamination down to ≤ 0.01 monolayers (ML), including the more persistent adventitious carbon, as judged by XPS. Ion sputtering preferentially removes lighter elements over heavier ones and thus preferentially removes S over Fe. A simple annealing procedure (370–570 K) alone could not generate defect-free surfaces and caused further removal of sulfur in the surface layer. However, defect-free and well-ordered surfaces could be obtained by annealing the sample in a controlled sulfur vapor ($\text{S}_2(\text{g})$) pressure of 1×10^{-7} Torr at 570 K for 10 min after which the sample was allowed to cool down to 370 K before the $\text{S}_2(\text{g})$ supply was shut off. A resistively heated W-wire wrapped around a Ta-foil-made crucible containing crushed pyrite was used as the $\text{S}_2(\text{g})$ source.

The 570 K annealing temperature was chosen to kinetically limit reduction of the sample induced by residual H_2 in the vacuum chamber as well as to limit thermal decomposition of the sample. When annealing pyrite in the absence of $\text{S}_2(\text{g})$ at temperatures ≥ 620 K, we found the sulfur depletion rate via H_2S production from the surface to be significant as judged by mass spectrometry ($m/z = 34$) and sulfur monomer formation (S_M) at a S 2p XPS binding energy of 160.95 eV.¹¹ Prolonged annealing of the sample at 620 K or annealing at higher temperatures led to decomposition of the pyrite sample into

pyrrhotite ($\text{Fe}_{1-x}\text{S}_x$) as observed by S 2p XPS and the evolution of a molecular S_2 ($m/z = 64$) mass spectrometer signal. These observations are consistent with previous experimental data on pyrite H-reduction and the thermal pyrite-to-pyrrhotite transformation.^{26–28}

3. RESULTS AND DISCUSSION

Soft X-ray S 2p XP spectra ($h\nu = 225$ eV) probing on the order of 5–10 Å deep and mainly sensitive to the first surface layer for different surface preparations are shown in Figure 2; in particular the S 2p XP spectrum from a sulfur dimer terminated and thus monomer-free surface is presented in Figure 2(a).

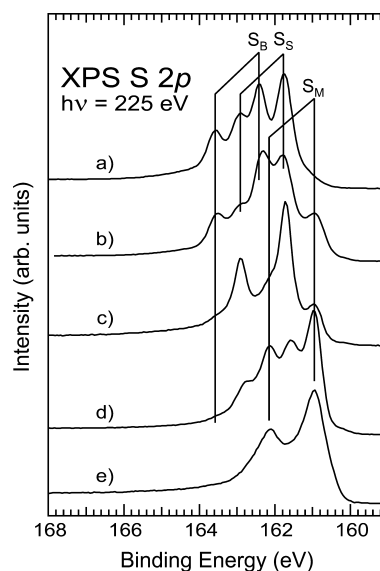


Figure 2. S 2p XP spectra from various treatments of the $\text{FeS}_2\{100\}$ surface correlated with LEED images in Figure 3(a)–(c). Total energy resolution is 100 meV. All spectra are normalized to the same area. Spectral fingerprints of species S_B , S_S , and S_M described in the text are marked in (a)–(d). (a) A sulfur dimer terminated surface and (b) low defect-density surface with sulfur monomers induced by 10 min of 200 V Ne^+ -sputtering. (c) S 2p XPS for a surface exposed to multiple sputter and anneal cycles without applying the anneal procedure in $\text{S}_2(\text{g})$, (d) highly sulfur-deficient surface induced by prolonged Ne^+ -sputtering of an initially defect-free surface, and (e) thermally decomposed pyrite (pyrrhotite $\text{Fe}_{1-x}\text{S}_x$).

The 162.35 and 161.75 eV $\text{S } 2p_{3/2}$ components with their corresponding $\text{S } 2p_{1/2}$ components at 1.19 eV higher binding energy (163.54 and 162.94 eV) are assigned to bulk-coordinated sulfur dimer atoms (S_B) with Fe-coordination number of three ($\text{Fe}_{\text{CN}} = 3$) and dimer sulfur atoms with reduced coordination number ($\text{Fe}_{\text{CN}} = 2$) at the vacuum interface (S_S), respectively, using the structural nomenclature and peak assignment in ref 11. No spectral signatures of monomeric adsulfur (S_A) ($\text{Fe}_{\text{CN}} = 1$), with an expected $\text{S } 2p_{3/2}$ XPS component at about 160.35 eV,¹¹ could be resolved for the sulfur dimer terminated surfaces. Sulfur dimer terminated surfaces with S 2p XP spectra as in Figure 2(a) displayed over the entire crystal surface area a novel single domain LEED pattern of apparent 2×1 symmetry as shown in Figure 3(a).

The 2×1 LEED pattern cannot be explained by simple kinematic scattering theory of bulk truncated sulfur dimer terminated surfaces, which results in a 1×1 symmetry, and will be discussed later. All LEED patterns observed in this work, the

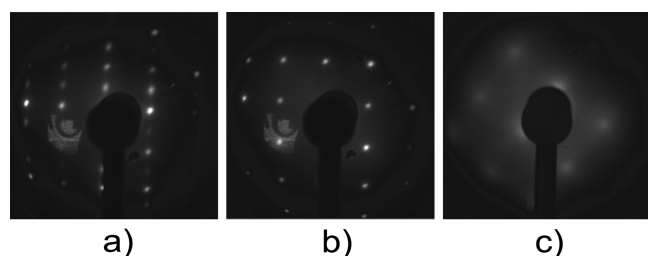


Figure 3. LEED images correlated with S 2p XP spectra in Figure 2(a)–(c). Electron beam kinetic energies were 110, 110, and 123 eV for (a), (b), and (c), respectively. (a) Sulfur dimer terminated surface displaying a single domain 2×1 LEED pattern, (b) low defect-density surface with sulfur monomers displaying the 1×1 LEED pattern, and (c) $(1/\sqrt{2} \times 1/\sqrt{2})R45^\circ$ LEED pattern from a surface exposed to multiple sputter and anneal cycles without applying the anneal procedure in $S_2(g)$. The LEED picture in (c) was recorded in an early separate run of experiments before (a) and (b), where the characteristic spots and scratches on the LEED optics in (a) and (b) were not yet present.

2×1 , as well as the 1×1 and $(1/\sqrt{2} \times 1/\sqrt{2})R45^\circ$ LEED patterns discussed later, were all very stable and showed no signs of electron-induced beam damage. This is in contrast to earlier work where LEED patterns degraded rapidly over the course of minutes for fracture-generated $FeS_2\{100\}$ surfaces.²⁹ Similarly, no change over time in S 2p XP spectra due to X-ray or electron-induced beam damage was observed.

We recognize that LEED spot intensities are sensitive to LEED geometry. As described in Section 2, our LEED studies were performed at $3\text{--}5^\circ$ off-axis (azimuthal) as our samples were mounted to allow for grazing photon incidence at the synchrotron. However, the slight off-axis geometry did, as expected, not affect the obtained LEED pattern symmetry. Remounting the samples rotated by 90° also produced a LEED pattern rotated by 90° . Similarly, variations in polar angle did not affect the symmetry of the LEED pattern for any of our surface preparations. We thus find that independent of sample orientation the 2×1 LEED pattern has its LEED (reciprocal space) short axis, i.e., real space long axis, aligned parallel to the narrow visible striations observed on the sample surface and thus parallel to the b -axis in Figure 1.

From S 2p XP spectra it was concluded that sulfur monomers in pyrite, S_M ($Fe_{CN} = 3$), with its S $2p_{3/2}$ component at 160.95 eV [Figures 2(b)–(d)], could be eliminated [Figure 2(a)] for the surface preparations in Figure 2(b)–(d) through the described annealing procedure in $S_2(g)$. Low defect density surfaces, which show S 2p XP spectra [Figure 2(b)] essentially identical to fracture-generated surfaces,^{10,14,15,30,31} exhibited the 1×1 LEED pattern in Figure 3(b). The formation of the 1×1 LEED pattern requires a well-ordered and (near) intact S_2^{2-} sublattice in the near surface region (see Figure 1(b) and 1(d)). This LEED pattern is identical to the LEED pattern from $FeS_2\{100\}$ surfaces prepared by fracture cleavage;^{29,31} note that this LEED pattern was labeled as $(\sqrt{2} \times \sqrt{2})R45^\circ$ in some previous works.^{29,31} Although a certain LEED spot broadening could be expected due to the limited but significant amounts of defects introduced, this can in our case not readily be observed. We simply note that fracture generated surfaces, with very similar defect densities as in Figure 2(b), also exhibit a similarly sharp 1×1 LEED pattern.^{29,31} From our XPS and LEED results it is apparent that the initially sulfur dimer terminated surfaces for which limited amounts of sulfur vacancies have

controllably been introduced by the gentle sputtering procedure are similar to fracture-generated surfaces at the local atomic structure scale probed by XPS and up to the 5–10 nm scale as probed by the coherence length of the LEED electron beam. We note that the thermal treatment of our samples, and them being natural growth surfaces, may both result in our surfaces being more irregular at the scale of tens of nanometers compared to fracture-generated surfaces,^{32,33} the consequence of which may be a higher step density on our surfaces compared to fracture-generated surfaces. However, similarly to our surfaces where the mild sputtering procedure ensures an even distribution of defects and thus that the majority of sulfur monomers is located on terrace sites, monomers on fracture-generated surfaces are also primarily located on terrace sites. The surface sulfur dimer to monomer ratio for fracture-generated $FeS_2\{100\}$ surfaces is on the basis of S 2p XPS data about three to four,^{10,14,15,30,31} i.e., sulfur atom vacancies leaving behind sulfur monomers make up 20–25% of all sulfur surface sites. Representative STM images for fracture-generated surfaces show a low step density with average spatial separation as large as 100 and 400 Å in different step density regions,²⁹ this corresponds to 2.7 and 0.7% step sites out of all surface sites, respectively. It is thus extremely unlikely that the relatively high density of monomers at fracture-generated $FeS_2\{100\}$ surfaces derives from step sites.

A surface exposed to multiple sputter and anneal cycles without applying $S_2(g)$ had the corresponding S 2p XP spectrum presented in Figure 2(c) and with LEED pattern as presented in Figure 3(c). Surface contamination is ruled out to affect the sulfur core-level shifts because surface C-, N-, and O-species were ≤ 0.01 ML as judged by XPS, and we estimate an upper limit of 0.03 ML surface H contamination from residual hydrogen based on the vacuum chamber base pressure (2×10^{-10} Torr) and the fairly short amount of time (≤ 15 min) before data acquisition after the final 570 K anneal. The real space lattice parameter was determined via analysis of the LEED patterns to be within 1% of factor $1/\sqrt{2}$ relative to the 1×1 structure, and the diffuse $(1/\sqrt{2} \times 1/\sqrt{2})R45^\circ$ LEED pattern is explained in terms of diffraction mainly from the cubic Fe ion sublattice (see Figure 1(b) and 1(d)), with a degree of disorder. This suggests a highly sulfur-deficient surface region, consistent with the preferential sputtering of sulfur. Depth profiling by photon energy dependent S 2p XP and valence band (VB) spectra (not shown) verified the presence of S_B -species and thus the underlying pyrite bulk structure but also a very pronounced surface metallicity compared to defect-free samples and a near complete lack of S $3s$ S–S σ bonding–antibonding splitting (10–20 eV binding energy region) in the near surface volume. The latter proves a very low concentration of surface sulfur dimers, consistent with the near negligible concentration of very near surface S_B -species in Figure 2(c). However, how can we then explain the S 2p XP spectrum in Figure 2(c) which suggests a low fraction of monomers (S_M) ($Fe_{CN} = 3$), very low fraction of bulk-coordinated dimer sulfur atoms (S_B) ($Fe_{CN} = 3$), and what appears to be a high fraction of dimer sulfur atoms with $Fe_{CN} = 2$ similar or identical to that found at the vacuum interface (S_S)?

The XPS results for the highly sulfur-deficient surfaces in Figures 2(c) and (d) can be explained by a high density of sulfur monomers having a higher Fe_{CN} value than in the pyrite structure ($Fe_{CN} = 3$). The XPS binding energy shift between sulfur in sulfur dimers with the Fe_{CN} value changing from two (S_S) to three (S_B) is about +0.65 eV.¹¹ Thus, the XPS binding

energy shifts upward by a significant amount by increased Fe coordination, and sulfur monomers with $\text{Fe}_{\text{CN}} = 4$ may therefore contribute the entire $\text{S } 2\text{p}_{3/2}$ XPS intensity near 161.7 eV, i.e., very near the binding energy of S_S . Indeed, sulfur monomers in mackinawite (tetragonal FeS) with an Fe–S distance the same as pyrite (2.26 Å)^{11,25,34,35} and with $\text{Fe}_{\text{CN}} = 4$ are shifted upward in binding energy by near 0.7 eV to $\text{S } 2\text{p}_{3/2}$ XPS binding energies around 161.65 eV as established from XPS and diffraction studies on mackinawite–greigite–pyrrhotite–pyrite interconversions.^{36,37} This may then also explain the XPS results for the extensively sputtered sample in Figure 2(d). A particularly interesting structure with identical bulk lattice parameter to pyrite (5.42 Å)^{34,38,39} is that of cubic FeS, the Fe–S end member of the sphalerite structure ($\text{Zn}_{1-x}\text{Fe}_x\text{S}$) which also has sulfur monomers with $\text{Fe}_{\text{CN}} = 4$ and similar Fe–S distance ($d_{\text{Fe-S}} = 2.35$ Å)^{38,39} to pyrite ($d_{\text{Fe-S}} = 2.26$ Å).^{25,34} As discussed later, this is a potential surface phase that can explain the 161.7 eV $\text{S } 2\text{p}_{3/2}$ XPS peak, as well as the $(1/\sqrt{2} \times 1/\sqrt{2})\text{R}45^\circ$ LEED pattern. A remark here based on our findings and discussion for the heavily defect surfaces is that there may be a certain spectral intensity contribution near S_S from monomeric sulfur with $\text{Fe}_{\text{CN}} = 4$ for the mildly sputtered 1×1 LEED pattern sample in Figure 2(b).

Either plausible FeS surface structure (cubic or tetragonal) is naturally devoid of sulfur dimers, and surface sulfur dimer vacancy sites may also be present for less sulfur-depleted surfaces locally remaining in the pyrite structure. This is especially true for surface monomer recombination around Fe vacancy sites where it clearly must be energetically favorable in cases when both monomers have suffered a loss in coordination due to the Fe vacancy and their recombination entails an overall gain of one S–S bond. Importantly, sulfur dimer vacancy sites are expected to be unique in their adsorption and reactivity properties.

Whether a FeS surface structure, e.g., cubic FeS commensurate with pyrite, can explain also the $(1/\sqrt{2} \times 1/\sqrt{2})\text{R}45^\circ$ LEED pattern is unclear. Monomeric sulfur in the pyrite structure (S_M) and what is assigned to monomeric sulfur in a FeS structure are both observed in the $\text{S } 2\text{p}$ XPS spectrum in Figure 2(c) related to the LEED pattern in Figure 3(c). The broad spot diffuse LEED pattern and its high background intensity may thus stem from a poorly long-range ordered cubic FeS surface structure commensurate with pyrite, just as well as it may stem from a poorly long-range ordered Fe backbone in a pyrite surface structure or a combination of both. On the basis of XPS data in ref 37 in combination with the poor surface order as judged by the LEED pattern, we can furthermore not exclude the new $\text{S } 2\text{p}_{3/2}$ XP spectral component at 161.7 eV to derive from a defective surface phase structurally resembling that of greigite (spinel Fe_3S_4) which also has sulfur monomers with $\text{Fe}_{\text{CN}} = 4$ and Fe–S distances of 2.21 and 2.42 Å.⁴⁰ We infer from our spectroscopical results and discussion, experimental as well as theoretical, that the explanation for the new $\text{S } 2\text{p}_{3/2}$ XPS component at 161.7 eV is a sulfur monomer with $\text{Fe}_{\text{CN}} = 4$, irrespective of whether its structural origin is highly defective pyrite or, e.g., greigite, cubic, or tetragonal FeS.

Pyrrhotite ($\text{Fe}_{1-x}\text{S}_x$) surfaces have previously been studied,⁴¹ and with respect to our pyrite samples thermally decomposed into pyrrhotite [Figure 2(e)], drastic changes in surface morphology were observed by visual inspection as a complete loss of the mirror finish of the pristine pyrite surface; no attempts to transform pyrrhotite back into pyrite were

performed. We note that neither in this case of sulfur depletion relative to pyrite nor for any of the other sulfur-depleted surfaces did we observe indications of a metallic Fe phase with S adsorbed displaying a $\text{S } 2\text{p}_{3/2}$ binding energy of 162.2 eV or higher.⁴²

Analyzing Fe/S XPS spectral intensity ratios we found that, as expected, the Fe:S ratio increases going from the dimer-rich to the monomer-rich terminations in Figure 2. Taking the dimer-terminated pyrite surfaces and pyrrhotite surfaces as reference points, at Fe:S = 1:2 and Fe:S \sim 0.9:1, respectively, we estimate that the defective FeS-like surface phase suggested for the data in Figure 2(c), correlating with the LEED pattern in Figure 3(c), is sulfur deficient and has an Fe:S ratio of about 3:2, a ratio higher than in pyrrhotite. Such a high Fe:S ratio is not unheard of, and several iron sulfide phases exist with high Fe:S ratios, with the end member structure being stable at atmospheric conditions and having a Fe:S ratio of 3:1.⁴³

Returning to the case of the apparent 2×1 LEED symmetry for sulfur dimer terminated surfaces, we below discuss its possible origin by considering various surface structural scenarios. Despite significant efforts to provide a coherent explanation for the 2×1 LEED pattern and corresponding $\text{S } 2\text{p}$ XP spectrum, we can at our present state of knowledge only leave it as an experimental observation that requires further study to determine its physical origin.

With respect to a possible superstructure of adsulfur atoms (S_A) inducing the 2×1 symmetry, these lower coordinated adsulfurs would be observed at 1.4 eV lower binding energy than the surface-most sulfur in the surface dimer (S_S),¹¹ and we see no evidence of such sulfur species in the $\text{S } 2\text{p}$ XP spectrum in Figure 2(a). Furthermore, the S_S to S_B spectral intensity ratio for the very surface-sensitive $\text{S } 2\text{p}$ XP spectra in Figure 2(a) and comparisons to pyrite $\text{FeS}_2\{100\}$ surfaces generated by fracturing^{10,14,15,30,31} do not immediately indicate a significant presence of any other special sulfur species at the surface which would coincidentally end up at the same binding energy as that of S_S (or, less likely, S_B), such as the newly discovered sulfur component for highly sulfur-deficient pyrite surfaces with its $\text{S } 2\text{p}_{3/2}$ XPS binding energy at 161.7 eV which we assign to monomeric sulfur with $\text{Fe}_{\text{CN}} = 4$. However, a smaller amount of some surface adsulfur species different from S_A and spectrally overlapping with the S_S component can not be entirely excluded. We note that, as was pointed out in our previous paper,¹¹ there is a small spectral intensity (10–15% of S_S) at 161.25 eV in Figure 2(a), which could possibly be due to a relatively high step density for our thermally treated natural growth surfaces (discussed earlier), Fe vacancies resulting in surface sulfur dimer atoms with $\text{Fe}_{\text{CN}} = 1$, and/or small amounts of stacking fault layers of a nature similar to the polymorph marcasite⁴⁴ present in our crystals. $\text{S } 2\text{p}$ XP spectral components of marcasite are not significantly different compared to pyrite, and the minor feature observed at 161.25 eV (1.1 eV below pyrite S_S) could then correspond to the nonreactive $\text{S } 2\text{p}$ XP spectral component found at marcasite surfaces generated by fracturing.⁴⁵ The small spectral intensity at 161.25 eV may thus correlate with the 2×1 LEED pattern via ordered Fe surface vacancies and/or marcasite-like stacking fault layers.

A possible surface reconstruction could also be envisaged to explain the LEED pattern for the dimer terminated surface. If the 2×1 LEED pattern for dimer-terminated (defect-free) surfaces would indeed be caused by a surface reconstruction, it has to be caused by only very small structural displacements

from a uniformly relaxed bulk-truncated pyrite {100} surface. We arrive at this by referring to the very good agreement of experimental S 2p core level shifts for the defect-free surface compared to modeled S 2p core level shifts for local sulfur structures at a structurally relaxed sulfur dimer terminated pyrite {100} surface.¹¹

To summarize, we can not pin down the origin of the 2×1 LEED pattern based solely on our XPS results. As discussed, however, it may be caused by smaller amounts of a hitherto unidentified adsulfur surface species different from S_A and spectrally overlapping with the already established S_S component, ordered surface Fe vacancies possibly combined with sulfur dimer vacancies, an ordering of marcasite-like stacking faults, or a surface reconstruction caused by only very small structural displacements from a uniformly relaxed bulk-truncated sulfur dimer terminated pyrite {100} surface.

In Figure 4(a)–(c) we summarize our main conclusions on the sulfur-related structural situations at the pyrite $FeS_2\{100\}$

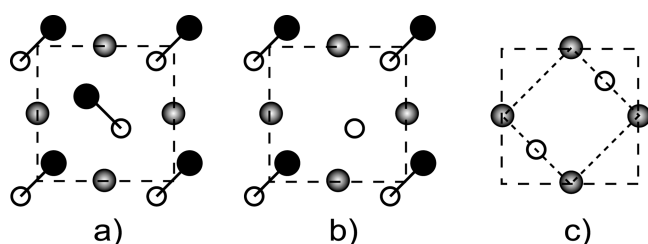


Figure 4. Illustrations of structural configurations at pyrite $FeS_2\{100\}$ surfaces depending on preparation and defect density as discussed in the text. (a) Defect-free surface, (b) sulfur atom vacancy leaving behind a monomeric sulfur, and (c) sulfur dimer vacancies and cubic $FeS\{100\}$ structure. In all three figures the surface unit cell of pyrite $FeS_2\{100\}$ is marked out with a longer dashed line. In the case of sulfur dimer vacancies and cubic $FeS\{100\}$ surface structure in (c), the smaller $(1/\sqrt{2} \times 1/\sqrt{2})R45^\circ$ surface unit cell is also marked out with a shorter dashed line. Gray filled circles represent Fe atoms; black filled circles represent sulfur atoms closest to the viewer; and unfilled circles represent sulfur atoms further away from the viewer.

surface consistent with crystal orientation of our samples, conditions of preparation, XPS and LEED results in Figure 2(a)–(c) and Figure 3(a)–(c), and structural properties of other Fe_xS_y minerals.

Going from the defect-free surface in Figure 4(a), a point-defect sulfur atom vacancy site¹¹ is shown in Figure 4(b) for the topmost FeS_2 layer surface unit cell. As shown in Figure 4(c) for Fe^{2+} and S^{2-} at the vacuum interface, here depicting the possible cubic FeS -like {100} surface phase commensurate with the pyrite Fe^{2+} sublattice, with increasing surface sulfur depletion, sulfur dimer vacancies are also introduced. If indeed our findings correspond to a cubic FeS surface phase, its inherent properties are likely a degree of nonstoichiometry, and thus necessarily disorder, as well as pronounced metastability and metallicity.^{38,39,46–48} Importantly, sulfur dimer vacancy sites formed either via monomer recombination in local regions of pyrite surface structure or as a result of a FeS surface phase are expected to be of a very reactive nature, with a possibility for 5-fold coordination to Fe atoms in this site: four in the surface plane and one in the layer below. In general, parallels to pyrite $FeS_2\{100\}$ surface defect site chemical activity may be drawn from sulfur-depleted pyrite $RuS_2\{100\}$ surfaces, highly active for catalytic reactions such as hydrodenitrogenation,

hydrodeoxygenation, hydrosulfurization, hydrogenation,⁴⁹ and thus naturally also active for the reverse reactions.

Compared to our results presented here, and other recent interesting studies on pyrite $FeS_2\{100\}$ surfaces,^{32,50,51} treatment of initially $S_2(g)$ -treated defect-free and/or fracture-cleaved surfaces by mild H_2 reduction at temperatures up to 570 K may induce well-defined defective sulfur-depleted surfaces with relevant S–H and Fe–H surface species for further surface science and catalysis studies.

4. CONCLUSIONS

To summarize our overall findings, we have established a procedure to generate sulfur dimer (S_2^{2-}) terminated pyrite $FeS_2\{100\}$ surfaces with a LEED pattern of 2×1 symmetry having its long real space axis parallel with the macroscopic striations on the pyrite cube face and thus, at the microscopic scale, parallel with the lattice-sulfur induced valley and trough structures at the anisotropic surface. The physical origin of the 2×1 LEED pattern is yet to be determined; it may be caused by smaller amounts of a hitherto unidentified adsulfur surface species spectrally overlapping with the already established S_S XPS component, ordered surface Fe vacancies possibly combined with sulfur dimer vacancies, an ordering of marcasite-like stacking faults, or a surface reconstruction caused by only very small structural displacements from a uniformly relaxed bulk-truncated sulfur dimer terminated pyrite {100} surface.

By a mild and controlled sputtering of the sulfur dimer terminated surfaces, surfaces very similar at a microscopic level to fracture-generated surfaces with its 1×1 LEED pattern and limited sulfur monomer (S^{2-}) concentrations were generated. With increasing sulfur removal, the observed $(1/\sqrt{2} \times 1/\sqrt{2})R45^\circ$ LEED pattern and XPS results indicate a highly sulfur-deficient near-surface region where extensive structural collapse into a surface phase with sulfur monomer Fe coordination number increase from three (as in pyrite) to four has taken place. The highly sulfur-deficient surface phase, as well as bond counting energetics for surface monomer recombination around Fe vacancy sites on pyrite $FeS_2\{100\}$, implies surface sulfur dimer vacancy sites with unique adsorption and reactivity properties. The physical origin of the 2×1 LEED pattern, as well as the reactivity of sulfur dimer vacancy sites, could favorably be clarified in the future by local techniques such as scanning tunneling microscopy (STM) and atomic force microscopy (AFM).

AUTHOR INFORMATION

Corresponding Author

*Tel.: +1 (650) 926 2233. Fax: +1 (650) 926 4100. E-mail: nilsson@slac.stanford.edu.

Notes

The authors declare no competing financial interest.

ACKNOWLEDGMENTS

This work was supported by NSF grant CHE-0089215, the Swedish Foundation for Strategic Research, the Swedish Natural Science Research Council, and the U.S. Department of Energy, Office of Basic Energy Sciences through Stanford Synchrotron Radiation Laboratory. The staff at MAX-lab is gratefully acknowledged.

REFERENCES

- (1) Murphy, R.; Strongin, D. R. Surface Reactivity of Pyrite and Related Sulfides. *Surf. Sci. Rep.* **2009**, *64*, 1–45.
- (2) Ennaoui, A.; Fiechter, S.; Pettenkofer, C.; Alonso-Vante, N.; Buker, K.; Bronold, M.; Hopfner, C.; Tributsch, H. Iron Disulfide for Solar Energy Conversion. *Sol. Energy Mater. Sol. Cells* **1993**, *29*, 289–370.
- (3) Nordstrom, D. K.; Alpers, C. N. Negative pH, Efflorescent Mineralogy, and Consequences for Environmental Restoration at the Iron Mountain Superfund Site, California. *Proc. Natl. Acad. Sci. U.S.A.* **1999**, *96*, 3455–3462.
- (4) Evangelou, V. P.; Zhang, Y. L. A Review: Pyrite Oxidation Mechanisms and Acid Mine Drainage Prevention. *Crit. Rev. Environ. Sci. Technol.* **1995**, *25*, 141–199.
- (5) Wächtershäuser, G. Before Enzymes and Templates: Theory of Surface Metabolism. *Microbiol. Rev.* **1988**, *52*, 452–484.
- (6) Wächtershäuser, G. Evolution of the First Metabolic Cycles. *Proc. Natl. Acad. Sci. U. S. A.* **1990**, *87*, 200–204.
- (7) Wächtershäuser, G. Groundworks for an Evolutionary Biochemistry: the Iron-Sulphur World. *Prog. Biophys. Mol. Biol.* **1992**, *58*, 85–201.
- (8) Sunagawa, I.; Endo, Y. Macro- and Micro-Morphology of Quartz and Pyrite. *IMA-Symposia, Mineral. Soc. London* **1968**, 63–84.
- (9) Endo, Y.; Sunagawa, I. Positive and Negative Striations in Pyrite. *Am. Mineral.* **1973**, *58*, 930–935.
- (10) Schaufuß, A. G.; Nesbitt, H. W.; Kartio, I.; Laajalehto, K.; Bancroft, G. M.; Szargan, R. Reactivity of Surface Chemical States on Fractured Pyrite. *Surf. Sci.* **1998**, *411*, 321–328.
- (11) Andersson, K.; Nyberg, M.; Ogasawara, H.; Nordlund, D.; Kendelewicz, T.; Doyle, C. S.; Brown, G. E., Jr.; Pettersson, L. G. M.; Nilsson, A. Experimental and Theoretical Characterization of the Structure of Defects at the Pyrite FeS₂(100) Surface. *Phys. Rev. B* **2004**, *70*, 195404.
- (12) Stirling, A.; Bernasconi, M.; Parrinello, M. Defective Pyrite (100) Surface: An Ab Initio Study. *Phys. Rev. B* **2007**, *75*, 165406.
- (13) Nair, N. N.; Schreiner, E.; Marx, D. Glycine at the Pyrite–Water Interface: The Role of Surface Defects. *J. Am. Chem. Soc.* **2006**, *128*, 13815–13826.
- (14) Nesbitt, H. W.; Bancroft, G. M.; Pratt, A. R.; Scaini, M. J. Sulfur and Iron Surface States on Fractured Pyrite Surfaces. *Am. Mineral.* **1998**, *83*, 1067–1076.
- (15) Kendelewicz, T.; Doyle, C. S.; Bostick, B. C.; Brown, G. E., Jr. Initial Oxidation of Fractured Surfaces of FeS₂(100) by Molecular Oxygen, Water Vapor, and Air. *Surf. Sci.* **2004**, *558*, 80–88.
- (16) Rosso, K. M.; Becker, U.; Hochella, M. F. Surface Defects and Self-Diffusion on Pyrite {100}: An Ultra-High Vacuum Scanning Tunneling Microscopy and Theoretical Modeling Study. *Am. Mineral.* **2000**, *85*, 1428–1436.
- (17) Krishnamoorthy, A.; Herbert, F. W.; Yip, S.; van Vliet, K. J.; Yildiz, B. Electronic States of Intrinsic Surface and Bulk Vacancies in FeS₂. *J. Phys.: Condens. Matter* **2012**, *25*, 045004.
- (18) de Leeuw, N. H.; Parker, S. C.; Sithole, H. M.; Ngoepe, P. E. Modeling the Surface Structure and Reactivity of Pyrite: Introducing a Potential Model for FeS₂. *J. Phys. Chem. B* **2000**, *104*, 7969–7976.
- (19) Philpott, M. R.; Goliney, I. Y.; Lin, T. T. Molecular Dynamics Simulation of Water in a Contact with an Iron Pyrite FeS₂ Surface. *J. Chem. Phys.* **2004**, *120*, 1943–1950.
- (20) Persson, I. Review: Adsorption of Ions and Molecules to Solid Surfaces in Connection with Flotation of Sulphide Minerals. *J. Coord. Chem.* **1994**, *32*, 261–342.
- (21) Murowchick, J. B.; Barnes, H. L. Effects of Temperature and Degree of Supersaturation on Pyrite Morphology. *Am. Mineral.* **1987**, *72*, 1241–1250.
- (22) Edwards, K. J.; Schrenk, M. O.; Hamers, R.; Banfield, J. F. Microbial Oxidation of Pyrite: Experiments Using Microorganisms from an Extreme Acidic Environment. *Am. Mineral.* **1998**, *83*, 1444–1453.
- (23) Bebić, J.; Schoonen, M. A. A. Pyrite Surface Interaction with Selected Organic Aqueous Species under Anoxic Conditions. *Geochem. Trans.* **2000**, *1*, 47–53.
- (24) Denecke, R.; Väterlein, P.; Bässler, M.; Wassdahl, N.; Butorin, S.; Nilsson, A.; Rubensson, J. E.; Nordgren, J.; Mårtensson, N.; Nyholm, R. Beamline I511 at MAX II, Capabilities and Performance. *J. Electron Spectrosc. Relat. Phenom.* **1999**, *101–103*, 971–977.
- (25) Bragg, W. L.; Claringbull, G. F. *Crystal Structures of Minerals*; Cornell Univ. Press: Ithaca, 1965; p 67.
- (26) Lambert, J. M., Jr.; Simkovich, G.; Walker, P. L., Jr. The Kinetics and Mechanism of the Pyrite-to-Pyrrhotite Transformation. *Metall. Mater. Trans. B* **1998**, *29*, 385–396.
- (27) Alonso-Vante, N.; Chatzitheodorou, G.; Fiechter, S.; Mgoduka, N.; Poulios, I.; Tributsch, H. Interfacial Behavior of Hydrogen-Treated Sulphur Deficient Pyrite (FeS_{2-x}). *Sol. Energy Mater.* **1988**, *18*, 9–21.
- (28) Hong, Y.; Fegley, B., Jr. The Kinetics and Mechanism of Pyrite Thermal Decomposition. *Ber. Bunsenges. Phys. Chem.* **1997**, *101*, 1870–1881.
- (29) Rosso, K. M.; Becker, U.; Hochella, M. F. Atomically Resolved Electronic Structure of Pyrite {100} Surfaces: An Experimental and Theoretical Investigation with Implications for Reactivity. *Am. Mineral.* **1999**, *84*, 1535–1548.
- (30) Leiro, J. A.; Mattila, S. S.; Laajalehto, K. XPS Study of the Sulphur 2p Spectra of Pyrite. *Surf. Sci.* **2003**, *547*, 157–161.
- (31) Pettenkofer, C.; Jaegermann, W.; Bronold, M. Site Specific Surface Interaction of Electron Donors and Acceptors on FeS₂(100) Cleavage Planes. *Ber. Bunsenges. Phys. Chem.* **1991**, *95*, 560–565.
- (32) Herbert, F. W.; Krishnamoorthy, A.; Ma, W.; Van Vliet, K. J.; Yildiz, B. Dynamics of Point Defect Formation, Clustering and Pit Initiation on the Pyrite Surface. *Electrochim. Acta* **2014**, *127*, 416–426.
- (33) Hochella, M. F., Jr.; Rakovan, J. F.; Rosso, K. M.; Bickmore, B. R.; Rufe, E. New Directions in Mineral Surface Geochemical Research Using Scanning Probe Microscopes. *ACS Symp. Ser.* **1998**, *715*, 37–56.
- (34) Bayliss, P. Crystal Structure Refinement of a Weakly Anisotropic Pyrite. *Am. Mineral.* **1977**, *62*, 1168–1172.
- (35) Lennie, A. R.; Redfern, S. A. T.; Schofield, P. F.; Vaughan, D. J. Synthesis and Rietveld Crystal Structure Refinement of Mackinawite, Tetragonal FeS. *Mineral. Mag.* **1995**, *59*, 677–683.
- (36) Boursiquot, S.; Mullet, M.; Abdelmoula, M.; Génin, J.-M.; Ehrhardt, J.-J. The Dry Oxidation of Tetragonal FeS_{1-x} Mackinawite. *Phys. Chem. Miner.* **2001**, *28*, 600–611.
- (37) Li, Y.; van Santen, R. A.; Weber, T. High-Temperature FeS–FeS₂ Solid-State Transitions: Reactions of Solid Mackinawite with Gaseous H₂S. *J. Solid State Chem.* **2008**, *181*, 3151–3162.
- (38) de Médicis, R. Cubic FeS, a Metastable Iron Sulfide. *Science* **1970**, *170*, 1191–1192.
- (39) Takeno, S.; Zōka, H.; Niihara, T. Metastable Cubic Iron Sulfide - With Special Reference to Mackinawite. *Am. Mineral.* **1970**, *55*, 1639–1649.
- (40) Chang, L.; Rainford, B. D.; Stewart, J. R.; Ritter, C.; Roberts, A. P.; Tang, Y.; Chen, Q. Magnetic Structure of Greigite (Fe₃S₄) Probed by Neutron Powder Diffraction and Polarized Neutron Diffraction. *J. Geophys. Res.* **2009**, *114*, B07101.
- (41) Becker, U.; Munz, A. W.; Lennie, A. R.; Thornton, G.; Vaughan, D. J. The Atomic and Electronic Structure of the (001) Surface of Monoclinic Pyrrhotite (Fe₇S₈) as Studied Using STM, LEED and Quantum Mechanical Calculations. *Surf. Sci.* **1997**, *389*, 66–87.
- (42) Panzner, G.; Egert, B. The Bonding State of Sulfur Segregated to α -Iron Surfaces and on Iron Sulfide Surfaces Studied by XPS, AES and ELS. *Surf. Sci.* **1984**, *144*, 651–664.
- (43) Fei, Y.; Li, J.; Bertka, C. M.; Prewitt, C. T. Structure Type and Bulk Modulus of Fe₃S, a New Iron-Sulfur Compound. *Am. Mineral.* **2000**, *85*, 1830–1833.
- (44) Dódony, I.; Pósfai, M.; Buseck, P. R. Structural Relationship Between Pyrite and Marcasite. *Am. Mineral.* **1996**, *81*, 119–125.
- (45) Uhlig, I.; Szargan, R.; Nesbitt, H. W.; Laajalehto, K. Surface States and Reactivity of Pyrite and Marcasite. *Appl. Surf. Sci.* **2001**, *179*, 222.

- (46) Murowchick, J. B.; Barnes, H. L. Formation of Cubic FeS. *Am. Mineral.* **1986**, *71*, 1243–1246.
- (47) Pósfai, M.; Buseck, P. R.; Bazylinski, D. A.; Frankel, R. B. Reaction Sequence of Iron Sulfide Minerals in Bacteria and Their Use as Biomarkers. *Science* **1998**, *280*, 880–883.
- (48) Devey, A.; de Leeuw, N. H. Density Functional Theory Study of the High- and Low-Temperature Phases of Cubic Iron Sulfide. *Phys. Rev. B* **2010**, *82*, 235112.
- (49) Breyse, M.; Furimsky, E.; Kasztelan, S.; Lacroix, M.; Perot, G. Hydrogen Activation by Transition Metal Sulfides. *Catal. Rev.* **2002**, *44*, 651–735.
- (50) Che, L.; Gardenghi, D. J.; Szilagyi, R. K.; Minton, T. K. Production of a Biomimetic Fe^(II)-S Phase on Pyrite by Atomic-Hydrogen Beam-Surface Reactive Scattering. *Langmuir* **2011**, *27*, 6814–6821.
- (51) Liu, T.; Temprano, I.; Jenkins, S. J.; King, D. A.; Driver, S. M. Low Temperature Synthesis of NH₃ from Atomic N and H at the Surfaces of FeS₂{100} Crystals. *J. Phys. Chem. C* **2013**, *117*, 10990–10998.